OPTICA

Low-cost electrothermally actuated MEMS mirrors for high-speed linear raster scanning

BIBEK R. SAMANTA,[1,*] **FLAVIO PARDO,**[1] **TODD SALAMON,**[1] **ROSE KOPF,**[1] **AND MICHAEL S. EGGLESTON**[1,2]

[1]*Nokia Bell Labs, 600 Mountain Ave, New Providence, New Jersey, 07974, USA*
[2]*e-mail: michael.eggleston@nokia-bell-labs.com*
Corresponding author: bibek.samanta@nokia-bell-labs.com

Electrothermally actuated MEMS mirrors are significantly lower in cost than their electrostatically actuated counterparts, largely due to their ability to perform well without hermetic packaging. However, their typical slower speeds, higher power requirement, and non-linear drive limit their widespread use. In this work, we address these limitations and achieve an electrothermally actuated MEMS mirror capable of reliable linear raster scanning at speeds up to 300 Hz with a large angular range of motion ($\pm 40°$ optical). A simple pulse design technique is used to achieve $\sim$99% scan linearity and correct for artifacts like overshoot and ringing. Furthermore, segmented polysilicon microheaters along the actuators are used for impedance matching to low-voltage electronics, resulting in lower power consumption and improved scan speed and angular range. These mirrors serve as an attractive option for low-cost and compact integrated beam-steering optical devices, and we demonstrate one such use case in an optical coherence tomography (OCT) system.   © 2022 Optica Publishing Group under the terms of the Optica Open Access Publishing Agreement

https://doi.org/10.1364/OPTICA.446407

1. INTRODUCTION

Micro-electro-mechanical systems (MEMS) technology is widely used for micromirrors where a laser beam needs to be steered over a physical space. Solutions for beam steering involve integrated optical phase arrays, which suffer from poor angular resolution and large cross talk [1,2], or electrostatic MEMS mirrors, which can be costly due to need for hermetic packaging and high-voltage control circuits [3]. In the 1980s and 1990s, these mirrors were primarily adopted in the telecommunications industry for large-scale optical switching networks [4,5]. Since then, because of advances in semiconductor manufacturing, this technology has been widely utilized in miniaturized display and projection technologies [6–9] including retinal scanning displays and head-up displays [10,11]. More recently, these MEMS mirrors have emerged as successful market drivers for high-resolution sensing and imaging [12–14] tasks with applications in ranging [15], composition analysis [16], and depth profiling [17]—replacing traditional bulky and high-power galvanometer scanners, and providing compact, low-cost, and low-power consuming solutions for high-speed beam steering. As a result, MEMS micromirrors are now widely used in volumetric imaging techniques like optical coherence tomography (OCT) and LIDAR [18–25].

A MEMS scanner's performance is governed by factors such as actuation mechanism, actuator size, and drive complexity [20,21]. While electrostatically actuated MEMS mirrors are more commonly used because of their reliability and lifetime, electrothermally actuated (ETA) MEMS can offer significant

advantages in certain applications [26]. ETA mirrors have lower costs associated with packaging and operation because they do not require packaging for long-term reliability, have simpler control electronics, and exhibit large deflection ranges [26,27].

In this paper, we demonstrate an ETA micromirror (see Fig. 1), suitable for 1D scan speeds of up to 300 Hz with a wide optical angular range of up to $\pm 40°$. The actuators are impedance matched for low-voltage electronics and can be driven using 3.3 V digital pulse width modulated (PWM) signals. We validate the mirror's bidirectional scanning using a benchtop swept-source OCT (SS-OCT) system for imaging. We achieve more than 5× faster linear raster scanning compared to some of the most recent work involving such ETA micromirrors, as summarized in Table 1.

2. DESIGN OF MEMS ACTUATORS

The scanning micromirror was fabricated using the PolyMUMPS wafer service process by MEMSCAP. The full fabrication steps [28] utilizing polysilicon (PolySi) surfaces, sacrificial silicon oxide layers, and metal layers are depicted in Fig. 1(b). The layout consists of four compliant Poly2 serpentine springs connecting the mirror to four actuators. Each actuator is a bilayer assembly consisting of Poly2 and CrAu metal layer with a stress gradient across its thickness [29]. Upon release, relaxation of the tensile stress in the metal layer results in an upward bend of the actuator legs, which suspends the mirror above the substrate. The MEMS chip is then placed on a hotplate at 200°C for 5 mins to anneal the actuators
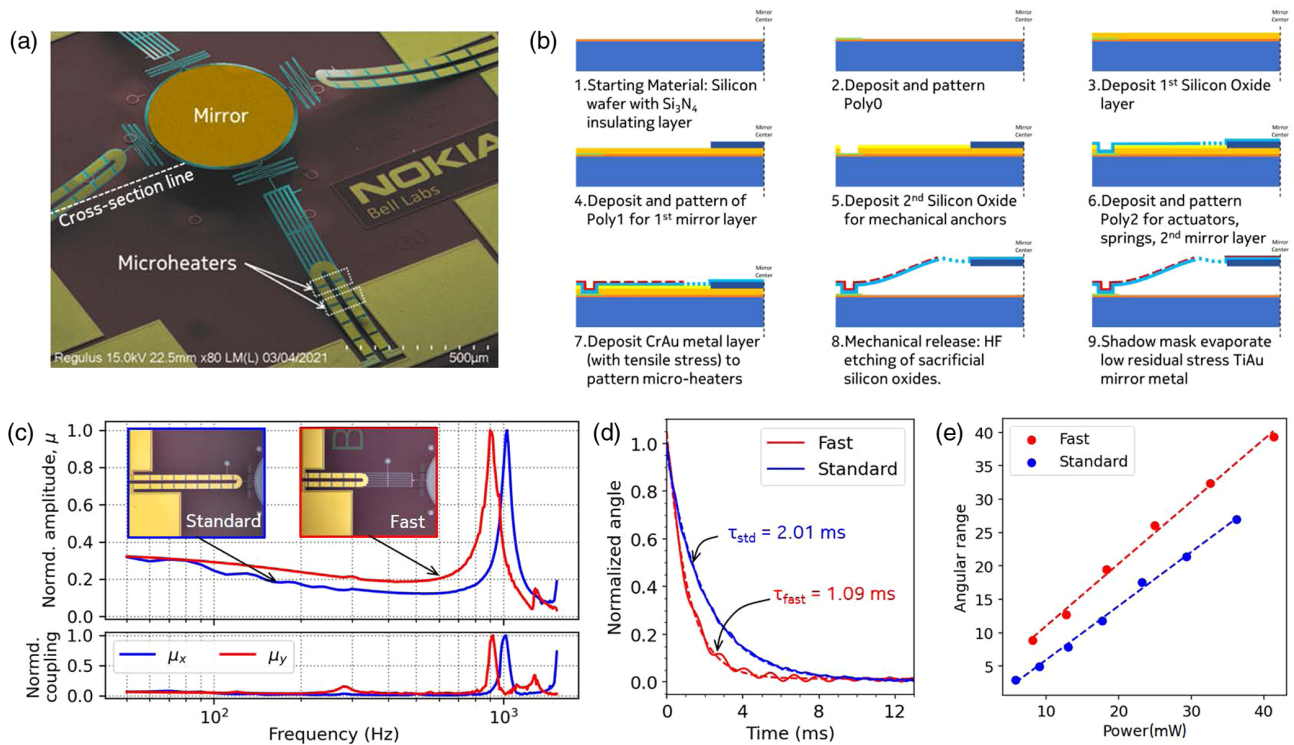
Fig. 1. (a) False-colored SEM image of the MEMS mirror with the PolySi microheaters highlighted. (b) Fabrication steps are shown along the dashed cross section line. (c) The normalized total moment of motion (or amplitude) is plotted (upper panel) against the input sinusoidal frequency for the *fast* and *standard* actuator designs, with their pre-release optical photographs shown in inset. The lower panel shows the coupling in the orthogonal direction, i.e., μ_y for X axis (fast actuators) and μ_x for Y axis (standard actuators) (d) The response of the actuators is fit to an exponential function with their time constants labeled. (e) The half-angular optical range is observed to be linearly dependent on input power.

Table 1.   Recent Electrothermally Actuated Micromirrors and Their Performance Metrics[a]

References	Dimensions	Angular Range (optical)	Operating Conditions	Reported Scan Speed/Times
Sun *et al.* [22]	1×1 mm^2	$\pm 30°$	16 mA, 5.5 V	1.25 Hz $\times$ 0.0125 Hz (raster scan)
Morrison *et al.* [30]	0.4 mm dia	$\pm 40°$	70 mA, 30 mW	5 ms (response time)
Zhou *et al.* [31]	1 mm dia	$\pm 8°$	2.35 V, 475 mW	7.3 ms (response time)
Wang *et al.* [24]	1.2×1.4 mm^2	$\pm 7°$	5 V, 55 mW	10 Hz $\times$ 1 Hz (raster scan)
Wang *et al.* [25]	0.5×0.5 mm^2	$\pm 12°$	6 V, -	50 Hz $\times$ 0.5 Hz (raster scan)
This work	0.5 mm dia	$\pm40°$	3.3 V, 40 mW	2.3 ms (response time), 250 Hz $\times$ 2.5 Hz (raster scan)

[a]We compare non-resonantly driven mirrors that report linear raster scanning or response time to a ramp.

to a final working mirror height of ~200 µm above the substrate. Serpentine structures have been reported earlier [30–32], and the basic actuation principle is similar to a previously reported design of a Poly1/Poly2 based 500 µm diameter mirror [30]. However, in this work, we utilize diametrically opposing actuator legs to minimize cross-axis coupling during raster scanning. In addition, our design incorporates high resistance microheaters along the actuator legs by stripping away 10 µm strips in the metal layer to expose the PolySi layer [see Fig. 1(a)]. By stripping away small sections of the metal layer, current is forced to travel through the much higher resistance PolySi layer. The impedance of the actuator can then be finely adjusted by changing the total length of exposed PolySi, allowing for impedance matching to low-voltage electronics. This reduces the drive current requirement and eliminates the requirements for an intermediate current regulation stage between actuator and drive source. Unlike the previous implementation [30], we do not use a metal layer on the mirror,

leaving the Poly1/Poly2 stack exposed. A standard PolyMUMPs Poly1/Poly2/metal stack would result in a rather high radius of curvature (~ 8 mm). Instead, we shadow-mask-evaporate a low-stress TiAu film on the released Poly1/Poly2 mirror, resulting in a flatter profile with a radius of curvature of approximately 100 mm.

The actuation principle is based on joule heating, realized due to a mismatch in the coefficient of thermal expansion of the Poly2 and metal layers, which flattens each actuator stack toward the substrate at about 40 mW power. The mirror can be driven in tip-tilt ($\pm40°$) and piston modes (~200 µm displacement; not utilized in this work) by using a suitable combination of time-varying electrical power dissipated along each actuator leg. During typical operation, we use opposite pairs of actuators for differential single-axis tip-tilt motion. Using Ansys, we simulated the rise time of different actuator lengths—600 µm, 450 µm, and 300 µm, assuming conduction through the substrate and air convection as the primary mode of heat dissipation. From this analysis, a

300 μm long actuator was predicted to have a time constant of 0.9 ms while a 600 μm long actuator had a time constant of 2.1 ms. Consequentially, we designed actuator pairs of different lengths for the two orthogonal axes as shown in Fig. 1. On the *standard* design, the microheaters are distributed evenly along the length of the 600 μm actuator. Faster actuation is achieved by keeping heat generation closer to the actuator's anchor with fewer microheaters along the 300 μm bilayer, while adding a frame-like extension to the other end to maintain the length of the mechanical lever arm to the mirror. Pre-release optical photographs of the *standard* and *fast* designs are shown in Fig. 1(c).

3. EXPERIMENTAL RESULTS

A. Mirror Characterization

The frequency response of the micromirror [in Fig. 1(c)] was evaluated by measuring the moment of motion, μ, determined by Eq. (1) around the geometric centroid, (x_c, y_c), of the scan pattern obtained on a position sensitive detector (PSD) under varying frequency excitations along each actuator pair,

$$\mu = \frac{\sum_{i=1}^{N} \left\{ \sqrt{(x_i - x_c)^2 + (y_i - y_c)^2} \right\}}{N}. \quad (1)$$

Here, index i represents all points from the scan trace in a single oscillation period of the sine drive, and the centroid is obtained using $(x_c, y_c) = ((\sum_i x_i)/N, (\sum_i y_i)/N)$. Although this method is similar to a doppler vibrometer measurement, one distinction is that it evaluates only the mirror motions which result in a net tip-tilt motion.

A resonance frequency at ∼1000 Hz, with a quality factor (Q) of ∼10, is observed for the mirror-spring system for both actuators. Because the standard actuator pair curl up more than the fast actuators upon release, the resonant mode for the connecting springs of the standard actuator, which get annealed in a stretched conformation, is observed at a slightly higher frequency most likely due to stress-stiffening. The rise times were measured by recording the actuators' response to a two-step pulse drive [33] and fit to an exponential as shown in Fig. 1(d). Because of the close-lying mechanical resonances of the two orthogonal axes, we observed increased cross-axis coupling at drive frequencies above 600 Hz leading to scan patterns that deviate from the intended line scanning. When driving both axes at two different frequencies, where both can be expressed as integer ratios, the mirror can be locked to scan in a Lissajous pattern. Although accessible, this scan mode is not utilized in this work due to the relative complexity of the resulting scan pattern and a non-uniform distribution of scan velocities. The time constants of the *standard* and *fast* actuators are 2.01 ms and 1.09 ms, respectively, which agrees well with our simulations, resulting in 10:90 rise times of 4.2 ms and 2.3 ms. The optical angular range measured along each axis using a differential 50 Hz sinusoidal drive (0–40 mW) was found to scale linearly with power. For the *standard* actuator the angular range increases linearly as ±0.74°/mW, and for the *fast* actuator we obtain ±0.93°/mW, achieving almost ±40° angular range. During a typical operation, we use the fast actuator pair for line scanning (here X axis), and the standard actuator pair (Y axis) completes the 2D raster scan [Fig. 2(a)]. To achieve maximum angular range, each actuator pair is differentially driven sinusoidally [see Fig 2(b)] or using optimally designed waveforms, as discussed in the next section.

Next, we consider the challenge of ensuring a uniform scan velocity during a single rectilinear sweep. A uniform scan velocity guarantees that the mirror sweeps linearly in time, i.e., intensity and residence time on each probe spot in the beam path are unvaried. Non-resonant high-speed drive can often result in overshoot and ringing, resulting from a high-Q mechanical resonance of the coupling or actuation mechanisms [24,34]. As a result, traditional control signals like linear ramps or single-step drive, which often encompass several high frequency components overlapping with this resonance, can lead to a non-uniform sweep velocity.

Tunable operation often involves a mirror redesign with re-optimized mechanical parameters, which can be non-trivial. In fact, Saleem *et al.* showed that performance and control of these mirrors involves several design constraints resulting in trade-offs between angular range, response time, and physical design parameters like mirror and/or actuator mass (or size), as presented in their multi-response optimization method [35]. For that reason, a less resource-intensive technique is required, which maximizes velocity uniformity and scan linearity at high speeds without compromising the angular range and duty cycle. We next demonstrate a control technique that achieves this using a simple pulse design method.

B. Linear Scan Control

Similar to the approach used by Imboden *et al.* [33], we use advanced pulse-shape control techniques to improve the step-and-settle response time. In this technique, the force applied during the turning points, or within a single half-oscillation period of the springs, is iteratively adjusted to approach the critical dissipation limit. As a result, the entire scan duration is composed of tunable steps that can be adjusted to minimize overshoot and ringing. The pulse design is then low-pass filtered to further minimize the possibility of exciting the mechanical resonance mode.

As shown in Fig. 2(c), the advanced multistep control of these MEMS devices consists of the following steps: (1) measure the mechanical resonance frequency (using a vibrometer or a PSD; here ∼1000 Hz), (2) use multiples of the half-period of one oscillation of the spring to derive the total scan time (e.g., eight steps for a 4 ms scan), (3) adjust the step amplitudes, (4) low-pass filter to block mechanical resonances and overtones (we filter >800 Hz), and finally (5) evaluate the resulting scan pattern and velocity distribution. A PSD is used for 2D position readout of the mirror's movement, generating a feedback that controls the resonant step amplitudes. In principle, we iteratively repeat steps 3 and 5 until the deviation in scan velocity through a forward sweep is below a minimum threshold (usually 20%). For the 2 ms forward sweep portion of a 250 Hz scan, while a sinusoidal drive can be considered uniform for only ∼0.8 ms for the set threshold, the optimized multistep drive yields uniform scan velocity for a 1.5 ms interval [Fig. 2(d)].

The key advantage of this technique is that it enables linear scanning at speeds higher than those limited by the mechanical resonance for conventional ramp techniques. As shown in Fig. 2(e), linear ramps with scan speeds faster than 125 Hz, about one-seventh of the resonant frequency, exhibit significant mechanical oscillations. These are especially pronounced in the 200 Hz scanning using a linear ramp (left panel). Previous work looking at the response times of similar thermally actuated mirrors concluded that the mirrors should ideally be driven at a cutoff frequency roughly one-tenth of the resonant frequency for a ringing-free
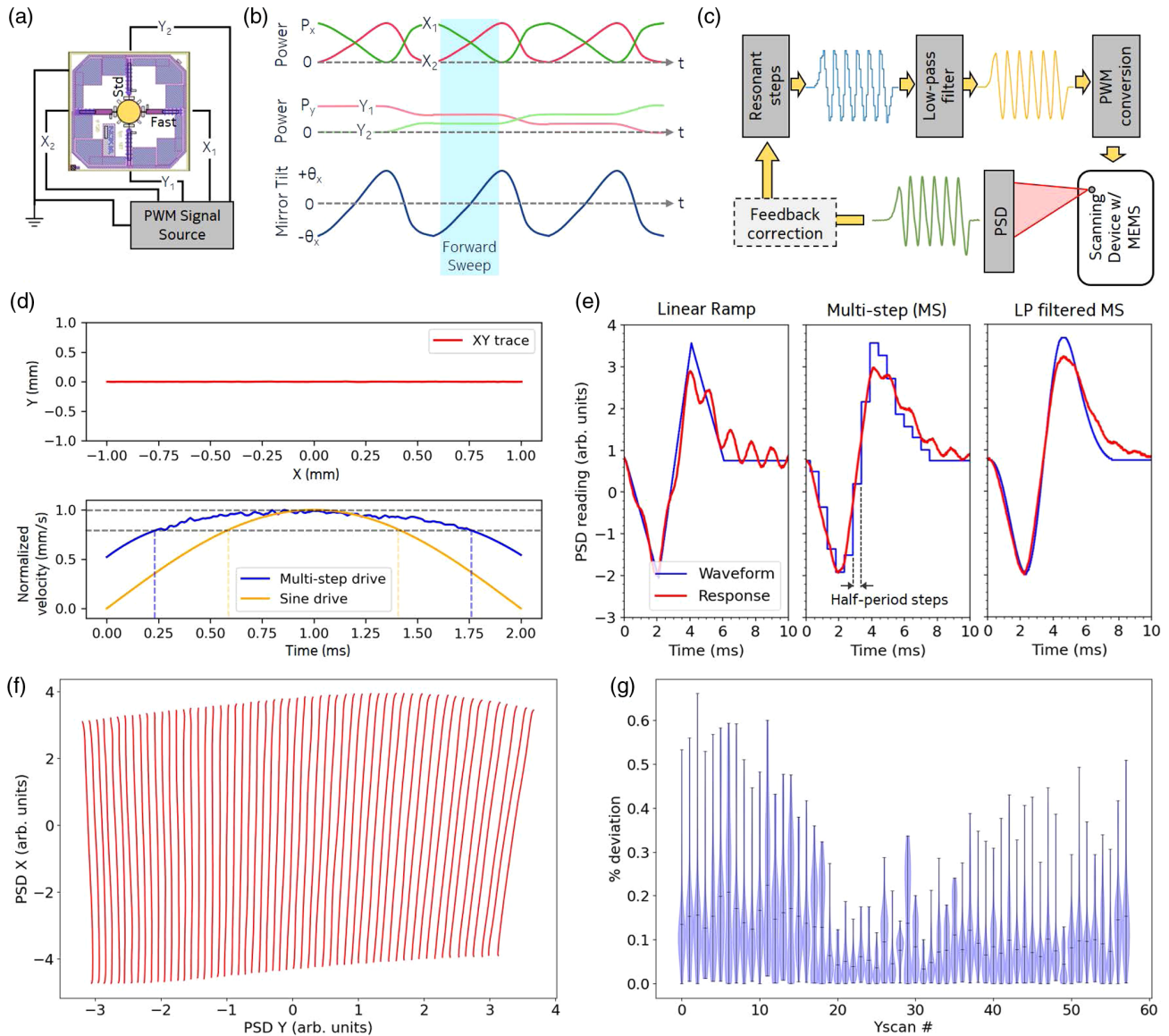
Fig. 2. (a) Schematic representation of the typical axes of scanning and (b) corresponding waveforms for raster scanning. (c) Schematic representation of the advanced multistep control design. (d) While both the multistep and sine drives yield the same PSD trace (upper panel), the former yields better velocity uniformity. (e) The three waveforms (linear, multistep, LP filtered multistep) are overlaid with their resulting scan patterns to highlight the contribution of ringing, and the half-period step used for waveform design is labeled. (f) A full 2D raster scan is obtained by repeating the optimized X-line scans while stepping Y axis power. (g) The relative deviation of each scan sweep from its intended straight line is characterized via a violin plot.

response [34], which for our mirrors would imply a 90 Hz operation. The multistep design can be applied to linearize the response at much faster timescales. In fact, at the same 200 Hz frequency, the multistep (middle panel) minimizes ringing and linearizes the forward sweep (2–4 ms). The low-pass filtered multistep drive smoothens the flyback sweeps (0–2 and 4–7 ms) as well. Using this technique, we could effectively optimize scans at speeds up to 300 Hz, almost one-third of the mechanical resonance.

We implement raster scanning by repeating the optimized 1D scans and stepping the orthogonal axis power during the flyback sweep. Because we scan in 2D using a single mirror mounted at a 45° angle relative to the incident beam, we observe a keystone effect in the 2D image as evident in the representative scan shown in Fig. 2(f). In the device shown, a slightly asymmetric release of the actuator pairs leads to additional distortions when approaching the scan extremes at full-range, as seen in the upper-right and

lower-left corners of the scan pattern. We further characterize the distortions arising from raster scanning by measuring the relative deviation of each raster from its intended straight line. The distribution of $\sigma_y^i/(X_{range}^i)$, which represents the standard deviation (or distortion) in the Y direction scaled by the total range of the ith line scan, is plotted in Fig. 2(g) for every i. We observe a maximum distortion of ~0.7%, and the average value over the entire 2D scan was ~0.2%.

C. Mirror Imaging Performance

Next, we use the mirror for imaging in a SS-OCT system. SS-OCT splits the light from a swept-wavelength laser into a fixed reference arm and a sample arm. The light reflected from different layers of the sample interfere with the reference beam resulting in an interferogram signal at the photodetector, from which the encoded
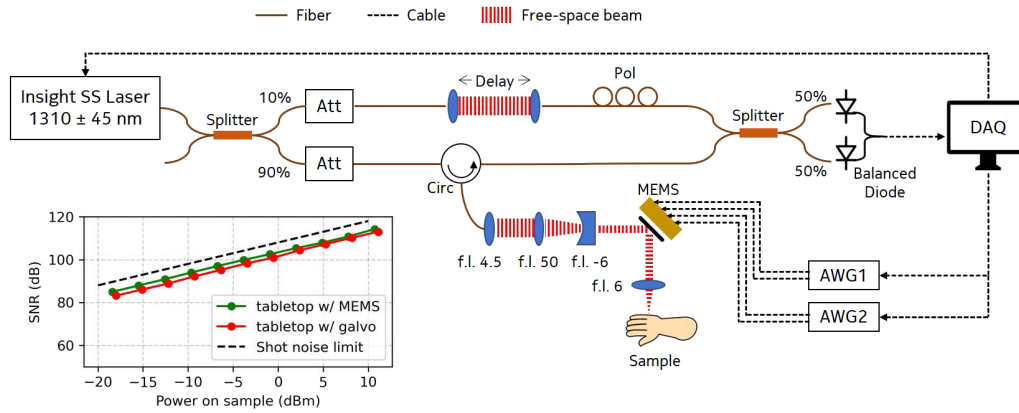
Fig. 3. SS-OCT system utilized for demonstrating transverse scanning in OCT using the MEMS mirror. Inset, sensitivity plot comparing system SNR as a function of power using a conventional galvo mirror setup (Thorlabs, NJ) versus our MEMS mirror. Focal length (f.l.) units are in mm.

depth information is obtained via a Fourier transform [36]. The MEMS mirror is integrated in the sample beam path for spatial scanning of the probe point on a 2D surface for a full 3D image. We employ an akinetic swept-source laser (Insight Photonic Solutions, Lafayette, Colorado) that has a center wavelength of 1310 nm and sweeps a full width at half-maximum bandwidth of about ~90 nm in k-space at 100 kHz, resulting in roughly 10 µm axial resolution in air. We replace the two single-axis galvo mirrors in our tabletop OCT system by the biaxially scanning MEMS mirror (see Fig. 3). The MEMS chip is wire bonded to a ceramic dual inline package, which is mounted on a breadboard for routing the PWM signals generated using two dual-channel arbitrary waveform generators. The MEMS mirror is used to perform 2D transverse scanning and is differentially driven using a 3.3 V PWM signal at 20 kHz, generated using the algorithm described in the previous section. The OCT signal is detected by a balanced photodetector pair, acquired by a DAQ card (GaGe CompuScope, Vitrek LLC, Lockport, IL) and processed on a computer. Our SNR measurements using a perfect reflector (Ag mirror) indicate no change compared to the galvo mirror assembly (Fig. 3, inset). The collimation lens assembly in the free space sample arm contributes to a single pass loss of 0.6 dB, and the loss after the final lens is measured to be close to 1 dB. The combined insertion losses at the circulator and at the 50:50 splitter input measured to be ~2.9 dB. The total loss of the light reflected from the sample arm is, therefore, estimated to be ~4.5 dB, which agrees well with the 4.47 dB lowered sensitivity compared to the shot-noise limit as shown in the SNR measurements in Fig. 3.

To demonstrate imaging performance, we obtained 3D OCT images with a field-of-view of roughly 3×3 mm^2 with an estimated lateral resolution of 30 µm. The power on sample for these images was close to 11 dBm. 2D scanning (line scan) is realized by differentially driving the fast actuators at a maximum power of 28 mW (to minimize distortions at max aperture stop) at 250 Hz. To demonstrate repeatability, we average 10 consecutive line scans to generate the image in Fig. 4(a) and find no noticeable blurring of features in the depth resolved layers of a 3M scotch tape reel over a 3 mm scan. The *en face* scan shown in Fig. 4(b) and 3D scans shown in Figs. 4(d)–4(f) are realized by repeating a single line scan 100 times, while differentially driving the standard actuators (slow axis) using a 2.5 Hz linear ramp at a maximum power of 28 mW, resulting in a scanned area of 3×2.8 mm^2. The lateral resolution of 30 µm is estimated from the beam divergence after the final scan lens, and the upper limit is verified using

a paper USAF chart [Fig. 4(b)] where we could resolve group 4 element 3 (20.2 lp/mm). We also demonstrate volumetric scanning on a fingertip [Figs. 4(d)–4(f)] where we could clearly see the dermal-epidermal junction, spiral sweat ducts, and fingerprint ridges.

D. Reliability and Lifetime

Next, to demonstrate the reliability of the MEMS micromirror for long-term operation, we also track the thermal drift and fatigue of the actuators. We subjected a fresh MEMS mirror to a continuous 200 Hz (a typical fast operation) differential sinusoidal drive for line scanning. While the mirror operated in continuous time for ~30 days, we recorded the scan extents at fixed intervals of time using a PSD. A plot of the normalized optical angular range against the number of cycles is shown in Fig. 5(a). There is a steady increase in angular range for the first one million cycles before it reaches a steady-state value. During this test, while in this "burn-in" period, the mirror's angular range increased from an initial ±20° to ~±27°. The range then stayed fairly constant until approximately 60 million cycles, after which the range slowly decreases until it reaches its pre-burn-in range of ~±20° after 200 million cycles. This gradual failure mode after rapid thermal cycling can be attributed to the formation of a PolySi-Au eutectic at the layer boundaries of the bimorph [37].

During this period, we also monitor the everyday scan-to-scan repeatability of the mirror response to the sinusoidal drive as well as the deviation from a straight line [see Fig. 5(b)]. The scan repeatability, quantified as $\sigma_X \langle (t) \rangle / X_{\text{range}}$, over a set of 100 continuous scans during a single day worsens from an initial 1.2% to only about 2% after 400 million cycles while the deviation from linearity, expressed as $\sigma_Y \langle (X) \rangle / X_{\text{range}}$, changes from an initial 0.014% to only about 0.018%.

To put these numbers in perspective, consider a scenario where the MEMS mirror is used in a handheld OCT device by an ophthalmologist. It would take approximately 50 years for a MEMS mirror on this device used for 100 volumetric scans a day to show noticeable signs for thermal fatigue. However, assuming a typical repair and upgrade period for modern day electronic devices, a period of 5 years would translate to an estimated 36 million cycles [vertical green line in Fig. 5(a)], which is well within the period of its normal operation.
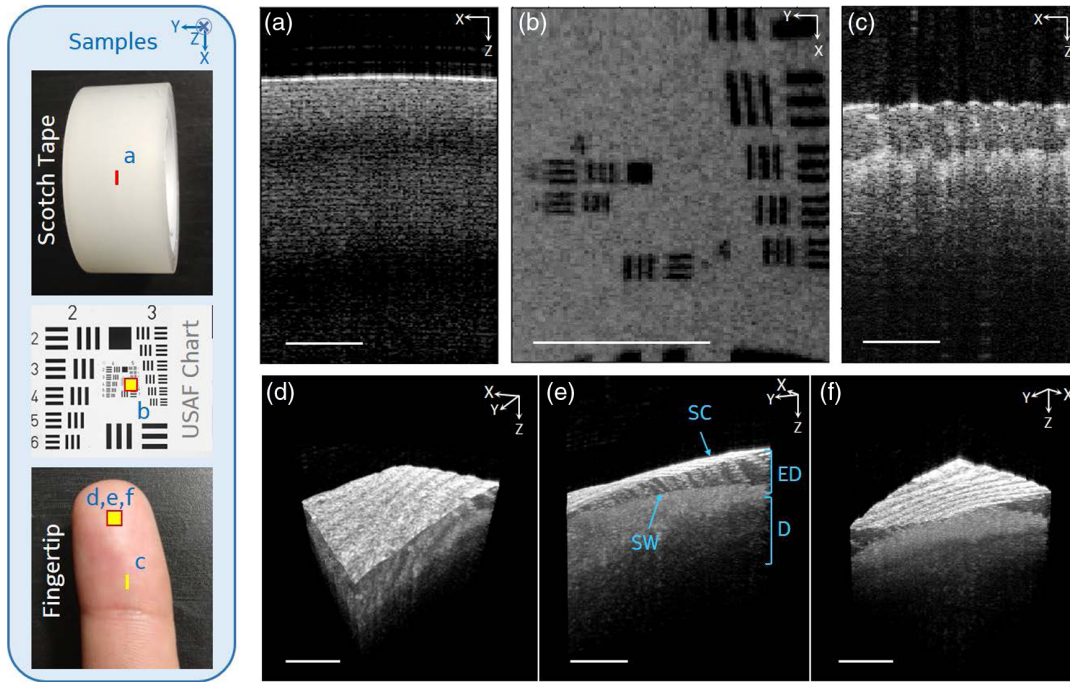
Fig. 4. Left panel shows the sample facets along with the scan extents and axes orientations corresponding to the OCT images shown in the right panels. (a) 10× averaged 2D cross section of a 3M scotch tape reel from a line scan. (b) *En face* image of USAF resolution chart. (c) B-scan of a fingertip, and (d)–(f) 3D volumetric images of a fingertip (BRS; right hand index finger). The scale bar in each figure represents 1 mm. SC, stratum corneum; SW, sweat duct; ED, epidermis; D, dermis.

4. CONCLUSION

Here we have a demonstrated an ETA MEMS mirror that operates under ambient atmosphere and does not need complex packaging
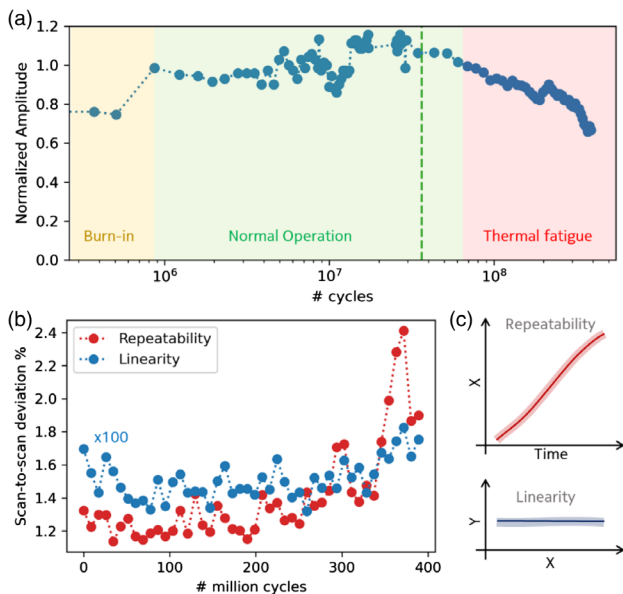

Fig. 5. (a) Semi-log plot of the mirror's scan amplitude for a 200 Hz sinusoidal drive over 400 million cycles. The green vertical line is an estimated typical use limit for a practical application (see text) (b) Scan-to-scan variation of scan repeatability and spatial linearity are plotted for the same time period to monitor the effect of thermal fatigue. The blue linearity trace has been multiplied by 100 for clarity. (c) The repeatability and linearity metrics over of set of 100 scans used in the text are depicted using an example diagram. The mean and standard deviation are represented by the solid line and shaded region, respectively.

steps. The mirror simultaneously achieves a wide optical angular range of $\pm40°$ and fast linear scanning at speeds up to 300 Hz. The key enabler for achieving uniform, linear, and ringing-free control at high speeds is the multistep pulse design technique introduced in this paper. As a result, these mirrors can be tuned to operate at different scan speeds and duty cycles. This technique encourages fast electrothermal actuation with time constants close to the mechanical resonance, with an automated feedback capability for pulse tuning and drive correction. In addition, these mirrors are impedance matched to work with low-voltage electronics without the need for additional bulky peripherals like high-voltage supplies or signal generators. Although the MEMS market is currently dominated by electrostatic mirrors, which are preferred for their high reliability, the low spatial footprint and easier packaging and integration capability position these electrothermal mirrors as a market-ready alternative for certain compact and wide-angle beam-steering applications like the recently developed chip-scale OCT system [38]. As a demonstration of the mirror's 2D high-speed linear raster scanning ability, we implement it on a benchtop OCT and control it with digitally generated 3.3 V PWM signals. The lifetime studies monitoring scan linearity and repeatability showed only a gradual drift when thermal cycled for more than a 300 million cycles at full power. Although these mirrors were fabricated using a standard foundry process, continued research is being done toward stabilizing metal alloys against fatigue [39], which can be included in the design optimization and further prolong the lifetime of electrothermal actuators. With our current low volume fabrication using the PolyMUMPS wafer service, we observe less than 20% deviation in the presented performance specs such as speed and angular range, and yields exceeding 60%. An optimized fabrication process for higher volumes can minimize such uniformity issues, improve yields, and lower fabrication costs.

REFERENCES

1. A. Yaacobi, D. Coolbaugh, G. Leake, J. Sun, M. R. Watts, and M. Moresco, "Integrated phased array for wide-angle beam steering," Opt. Lett. **39**, 4575–4578 (2014).
2. H. Rogier, K. Van Acoleyen, and R. Baets, "Two-dimensional optical phased array antenna on silicon-on-insulator," Opt. Express **18**, 13655–13660 (2010).
3. H. D. Tholl, "Novel laser beam steering techniques," Proc. SPIE **6397**, 639708 (2006).
4. D. J. Bishop, C. R. Giles, and G. P. Austin, "The Lucent LambdaRouter: MEMS technology of the future here today," IEEE Commun. Mag. **40**(3), 75–79 (2002).
5. Y. An, B. Sun, P. Wang, L. Xiao, H. Liu, and H. Xie, "A 1×20 MEMS mirror array with large scan angle and low driving voltage for optical wavelength-selective switches," Sens. Actuators A **324**, 112689 (2021).
6. M. K. Hedili, M. O. Freeman, and H. Urey, "Microstructured head-up display screen for automotive applications," Proc. SPIE **8248**, 84280X (2012).
7. H. Liao, "Super long viewing distance light homogeneous emitting three-dimensional display," Sci. Rep. **5**, 9532 (2015).
8. J. P. La Torre, N. A. Riza, and N. Mayes, "Laser display system for multi-depth screen projection scenarios," Appl. Opt. **56**, 9023–9029 (2017).
9. A. C. L. Hung, H. Y. H. Lai, T. W. Lin, S. G. Fu, and M. S. C. Lu, "An electrostatically driven 2D micro-scanning mirror with capacitive sensing for projection display," Sensors Actuators A **222**, 122–129 (2015).
10. M. Wagner, T. North, S. Bourquin, and L. Kilcher, "Lightweight high-brightness helmet-mounted head-up display system," Proc. SPIE **9770**, 97700F (2016).
11. V. Milanovic, A. Kasturi, and V. Hachtel, "High brightness MEMS mirror based head-up display (HUD) modules with wireless data streaming capability," Proc. SPIE **9375**, 93750A (2015).
12. Y. Seo, K. Hwang, and K. Jeong, "1.65 mm diameter forward-viewing confocal endomicroscopic catheter using a flip-chip bonded electrothermal MEMS fiber scanner," Opt. Express **26**, 4780–4785 (2018).
13. L. Y. Lin, E. G. Keeler, F. Chollet, and H. Jiang, "Progress of MEMS scanning micromirrors for optical bio-imaging," Micromachines **6**, 1675–1689 (2015).
14. C. Song, H. Guo, H. Xie, and L. Xi, "Photoacoustic endomicroscopy based on a MEMS scanning mirror," Opt. Lett. **42**, 4615–4618 (2017).
15. T. Sandner, M. Wildenhain, C. Gerwig, H. Schenk, S. Schwarzer, and H. Wölfelschneider, "Large aperture MEMS scanner module for 3D distance measurement," Proc. SPIE **7594**, 75940D (2010).
16. W. Wang, J. Chen, A. S. Zivkovic, and H. Xie, "A Fourier transform spectrometer based on an electrothermal MEMS mirror with improved linear scan range," Sensors **16**, 1611 (2016).
17. L. Liu, E. Wang, X. Zhang, W. Liang, X. Li, and H. Xie, "MEMS-based 3D confocal scanning microendoscope using MEMS scanners for both lateral and axial scan," Sens. Actuators A **215**, 89–95 (2014).
18. A. Kasturi, V. Milanović, D. Lovell, F. Hu, D. Ho, Y. Su, and L. Ristic, "Comparison of MEMS mirror LiDAR architectures," Proc. SPIE **11293**, 112930B (2020).
19. V. Milanović, A. Kasturi, J. Yang, and F. Hu, "Closed-loop control of gimbal-less MEMS mirrors for increased bandwidth in LiDAR applications," Proc. SPIE **10191**, 101910N (2017).
20. D. Wang, C. Watkins, and H. Xie, "MEMS mirrors for LiDAR: a review," Micromachines **11**, 456 (2020).
21. C. Gorecki and S. Bargiel, "MEMS scanning mirrors for optical coherence tomography," Photonics **8**, 1–25 (2021).
22. J. Sun, S. Guo, L. Wu, L. Liu, S.-W. Choe, B. S. Sorg, and H. Xie, "3D in vivo optical coherence tomography based on a low-voltage, large-scan-range 2D MEMS mirror," Opt. Express **18**, 12065–12075 (2010).
23. C. D. Lu, M. F. Kraus, B. Potsaid, J. J. Liu, W. Choi, V. Jayaraman, A. E. Cable, J. Hornegger, J. S. Duker, and J. G. Fujimoto, "Handheld ultra-high speed swept source optical coherence tomography instrument using a MEMS scanning mirror," Biomed. Opt. Express **5**, 293–311 (2014).
24. D. Wang, L. Thomas, S. Koppal, Y. Ding, and H. Xie, "A low-voltage, low-current, digital-driven MEMS mirror for low-power LiDAR," IEEE Sens. Lett. **4**, 5000604 (2020).
25. D. Wang, J. Zhang, L. Liu, Z. Yan, P. Wang, Y. Ding, and H. Xie, "Application of OCT for osteonecrosis using an endoscopic probe based on an electrothermal MEMS scanning mirror," Int. J. Optomechatron. **15**, 87–96 (2021).
26. A. Potekhina and C. Wang, "Review of electrothermal actuators and applications," Actuators **8**, 69 (2019).
27. E. Pengwang, K. Rabenorosoa, M. Rakotondrabe, and N. Andreff, "Scanning micromirror platform based on MEMS technology for medical application," Micromachines **7**, 24 (2016).
28. A. Cowen, B. Hardy, R. Mahadevan, and S. Wilcenski, *PolyMUMPs Design Handbook a MUMPs Process* (1992).
29. MEMSCAP, "Reference material and MEMS multi project wafer service," http://www.memscap.com/__data/assets/excel_doc/0018/1728/PolyMUMPs.rundata-web.xlsx.
30. J. Morrison, M. Imboden, T. D. C. Little, and D. J. Bishop, "Electrothermally actuated tip-tilt-piston micromirror with integrated varifocal capability," Opt. Express **23**, 9555–9566 (2015).
31. L. Zhou, X. Zhang, and H. Xie, "An electrothermal Cu/W bimorph tip-tilt-piston MEMS mirror with high reliability," Micromachines **10**, 323 (2019).
32. L. Zhou, X. Yu, P. X.-L. Feng, J. Li, and H. Xie, "A MEMS lens scanner based on serpentine electrothermal bimorph actuators for large axial tuning," Opt. Express **28**, 23439–23453 (2020).
33. M. Imboden, J. Chang, C. Pollock, E. Lowell, M. Akbulut, J. Morrison, T. Stark, T. G. Bifano, and D. J. Bishop, "High-speed control of electromechanical transduction: advanced drive techniques for optimized step-and-settle response of MEMS micromirrors," IEEE Control Syst. **36**, 48–76 (2016).
34. M. Li, Q. Chen, Y. Liu, Y. Ding, and H. Xie, "Modelling and experimental verification of step response overshoot removal in electrothermally-actuated MEMS mirrors," Micromachines **8**, 289 (2017).
35. M. M. Saleem, U. Farooq, U. Izhar, and U. S. Khan, "Multi-response optimization of electrothermal micromirror using desirability function-based response surface methodology," Micromachines **8**, 107 (2017).
36. E. A. Swanson, J. G. Fujimoto, and S. R. Chinn, "Optical coherence tomography using a frequency-tunable optical source," Opt. Lett. **22**, 340–342 (1997).
37. K. Gall, M. L. Dunn, Y. Zhang, and B. A. Corff, "Thermal cycling response of layered gold/polysilicon MEMS structures," Mech. Mater. **36**, 45–55 (2004).
38. M. S. Eggleston, F. Pardo, C. Bolle, B. Farah, N. Fontaine, H. Safar, M. Cappuzzo, C. Pollock, D. J. Bishop, and M. P. Earnshaw, "90 dB sensitivity in a chip-scale swept-source optical coherence tomography system," in *Conference on Lasers and Electro-Optics* (2018), paper JTh5C.8.
39. Y. Li, Q. Song, S. Feng, and C. Sun, "Effects of loading frequency and specimen geometry on high cycle and very high cycle fatigue life of a high strength titanium alloy," Material **11**, 1628 (2018).